

Late-time quadratic growth in single-mode Rayleigh-Taylor instabilityTie Wei^{*,†} and Daniel Livescu[‡]*Los Alamos National Laboratory, Los Alamos, New Mexico 87544, USA*

(Received 17 April 2012; revised manuscript received 23 July 2012; published 22 October 2012)

The growth of the two-dimensional single-mode Rayleigh-Taylor instability (RTI) at low Atwood number ($A = 0.04$) is investigated using Direct Numerical Simulations. The main result of the paper is that, at long times and sufficiently high Reynolds numbers, the bubble acceleration becomes stationary, indicating mean quadratic growth. This is contrary to the general belief that single-mode Rayleigh-Taylor instability reaches a constant bubble velocity at long times. At unity Schmidt number, the development of the instability is strongly influenced by the perturbation Reynolds number, defined as $Re_p \equiv \lambda\sqrt{Ag\lambda/(1+A)}/\nu$. Thus, the instability undergoes different growth stages at low and high Re_p . A new stage, chaotic development, was found at sufficiently high Re_p values, after the reacceleration stage. During the chaotic stage, the instability experiences seemingly random acceleration and deceleration phases, as a result of complex vortical motions, with strong dependence on the initial perturbation shape (i.e., wavelength, amplitude, and diffusion thickness). Nevertheless, our results show that the mean acceleration of the bubble front becomes constant at late times, with little influence from the initial shape of the interface. As Re_p is lowered to small values, the later instability stages, chaotic development, reacceleration, potential flow growth, and even the exponential growth described by linear stability theory, are subsequently no longer reached. Therefore, the results suggest a minimum Reynolds number and a minimum development time necessary to achieve all stages of single-mode RTI development, requirements which were not satisfied in the previous studies of single-mode RTI.

DOI: [10.1103/PhysRevE.86.046405](https://doi.org/10.1103/PhysRevE.86.046405)

PACS number(s): 52.35.Py

I. INTRODUCTION

Rayleigh-Taylor instability (RTI) is an interfacial instability that occurs when a high-density fluid is accelerated or supported against gravity by a low-density fluid. This instability is of fundamental importance in a multitude of applications, from fluidized beds, oceans, and atmosphere, to inertial or magnetic confinement fusion, and to astrophysics. The interface between the two fluids is unstable to any perturbation with a wavelength larger than the cutoff due to surface tension (for the immiscible case) or mass diffusion (for the miscible case). In this case, small perturbations grow to large amplitudes. At early times, if the initial perturbation amplitudes are small compared to their wavelength and the growth is not dominated by diffusive effects, the flow can be described by the linearized equations and the amplitudes grow exponentially with time. Later, the nonlinear effects become important and smaller and larger wave numbers are generated by nonlinear interactions. The interface evolves into bubbles of lighter fluid and spikes of heavier fluid penetrating the opposed fluid. There is a complex phenomenology associated with the evolution of RTI, including formation, competition, and amalgamation of spikes and bubbles, entrainment, and, eventually, turbulence.

Although RTI has been subjected to intense research over the last 50 years, a large number of open questions remain unanswered about this instability and even first order global quantities are not completely understood and still give rise to intense debate [1–3]. Before the 1980s, most RTI studies were either experimental or analytical. However, it is

notoriously difficult, in laboratory experiments, to accurately characterize the initial conditions and provide the detailed measurements needed for turbulence model development and validation. More recently, with the advance in supercomputer power, numerical simulations are becoming an ever more important tool in the study of RTI [4]. Nevertheless, many of the earlier numerical studies report growth rates which are significantly lower than those obtained in many experiments. Recent simulations suggest that the difference is due to low wave number perturbations inherent in many RTI experimental approaches [2,3,5]. Thus, given the difficulty in controlling the initial conditions in laboratory experiments, high-resolution Direct Numerical Simulations (DNS) of RTI, enabled by the present generation of supercomputers, becomes a natural tool for exploring such hypotheses and, eventually, settling the open questions regarding RTI.

Using DNS, we have systematically studied the development and dependence on initial conditions of single-mode RTI. This is a type of RTI which starts with a single-mode initial perturbation. Single-mode RTI presents symmetries in the initial conditions which the flow has to preserve at all times. Thus, the tips of the bubbles and spikes always lie along the symmetry lines. In addition, the initial wavelength is always preserved, as the distance between these symmetry lines, and the corresponding mode dominates at all times. Besides its own interest, single-mode RTI has also been used as a building block for the study of multimode RTI development (e.g., Ref. [6]). Despite its apparent simplicity, single-mode RTI is still not well understood and continues to be the focus of research in experimental (e.g., with two-dimensional (2D) perturbations [7–10] and three-dimensional (3D) perturbations [8]), numerical [11–15], and theoretical [16] studies. In the previous experimental studies, the duration of the instability evolution is relatively short ($H_B/\lambda \leq 1$), while numerical simulations with longer development time have relatively low

^{*}twei@nmt.edu[†]Present address: New Mexico Tech, Socorro, New Mexico 87801, USA.[‡]livescu@lanl.gov

Reynolds numbers, and a complete picture of the instability evolution is still lacking. For example, the bubble front has been thought to approach and maintain a constant “terminal velocity” at late times (i.e., linear bubble height growth, $H_B \sim t$), based on the assumption that the flow remains potential near the tip of the bubble. However, while the vorticity is zero in this region due to symmetry conditions, the induced velocities due to vortical motions inside the bubble become strong enough to render such potential flow solutions inadequate at long times, as our results below show. Nevertheless, many models for the growth of multimode RTI still use in some form the potential flow hypothesis.

In the earlier experimental studies, due to the size limitations of the facilities ($H_B/\lambda < 1$), the bubble front velocity seemed constant near the end of the measurements. However, Glimm *et al.* [12] and Ramaprabhu *et al.* [13] performed longer numerical simulations ($H_B/\lambda \approx 2$) and showed that the bubble front undergoes a reacceleration after its velocity reaches a plateau. This reacceleration was then confirmed experimentally by Wilkinson *et al.* [8], using a longer experimental apparatus. Nevertheless, it is not clear how long the reacceleration should last and what happens at longer times at high Reynolds numbers. For example, the recent low-resolution results of Ramaprabhu *et al.* [15] seem to show a return to linear growth. The results presented here point to a different picture at high Reynolds numbers.

The previous simulations of single-mode RTI are mostly Implicit Large Eddy Simulations (ILES) and, to the best of our knowledge, no Direct Numerical Simulations (i.e., using physical molecular transport properties and resolving all dynamically relevant scales) have been reported for this problem. The distinction is important since, as our results show, complex vortical motions dominate the late-time evolution, and good small-scale resolution is important to capture the vortical interactions. For example, using ILES, Ramaprabhu *et al.* [15] conducted simulations of 3D single-mode RTI, covering a wide range of Atwood numbers, with cross-sectional meshes from 8^2 to 128^2 . They report that the reacceleration stage cannot last forever (which is consistent with our simulations), and the flow transitions into a new stage, which they named “chaotic mixing.” During this “chaotic mixing” stage, the lines of symmetry within the bubbles and spikes of single-mode RTI, which the flow should preserve, are broken in their simulations. While we also call the late-time regime revealed by our results as “chaotic development,” this is different than the “chaotic mixing” regime in the Ramaprabhu *et al.* [15] study. Thus, our results (which do maintain the flow symmetries at all times) show that, at high enough Reynolds numbers, the bubble acceleration becomes stationary, with large fluctuations and nonzero average, corresponding to mean quadratic growth. The late-time bubble and spike velocities presented in Ramaprabhu *et al.* [15] are not chaotic and decrease lower than the “potential flow velocity.” Differences between 2D and 3D cases notwithstanding, our results show a similar behavior for the bubble acceleration at low Reynolds number values (see Sec. III C2). Our designation of “chaotic development” regime refers only to the high Reynolds number, late-time quadratic growth stage, which was not seen in Ref. [15].

Here, the first fully resolved simulations of single-mode RTI are presented. A more complete picture of the growth stages

in single-mode RTI has been revealed by these simulations, especially the presence of a new stage, chaotic development (CD), which occurs after the reacceleration stage. Our results show that single-mode RTI undergoes different growth stages as the Reynolds number increases from small to large values. Therefore, the results suggest a minimum Reynolds number (and a minimum numerical resolution) necessary to observe all stages of single-mode RTI development. This condition was not satisfied in the previous numerical simulations of single-mode RTI. Also lacking in the previous studies is a systematic investigation of the effects of the Reynolds number and initial perturbation shape (i.e., wavelength, amplitude, and diffusion thickness). Thus, the thickness of the initial diffusion layer and amplitude of the perturbation vary considerably among experiments and simulations of single- and multimode RTI. In order to understand the differences among these studies, we have also investigated the role of the initial perturbation shape on the instability development. All the simulations presented here are 2D.

The rest of the paper is organized as follows. Section II gives a brief description of the governing equations and numerical methodology. In the results Sec. III, the evolution of the instability at high-perturbation Reynolds number is first examined, followed by a discussion of the effects of the perturbation Reynolds number and the mean growth of instability in the new, chaotic development stage. The last part of the results section addresses the role of perturbation shape on the instability evolution. Section IV gives a summary of findings and conclusions. In the Appendix the verification and validation of the numerical approach are presented.

II. GOVERNING EQUATIONS AND NUMERICAL METHODOLOGY

A. Governing equations

In this paper we restrict our attention to miscible incompressible materials. Thus, the two pure fluids have constant, but different, microscopic densities. In this case, the specific volume and density of the mixture are related to the microscopic densities, ρ_l , and mass fractions, Y_l , by [4]

$$v = \frac{1}{\rho} = \frac{Y_H}{\rho_H} + \frac{Y_L}{\rho_L}, \quad (2.1)$$

which simply states that the total mass inside a control volume is the sum of the masses of the two fluids. The index $l = H, L$ refers to the pure heavy and light fluids, respectively, and $Y_H + Y_L = 1$. Although the Atwood number considered here is small ($A \equiv \frac{\rho_H - \rho_L}{\rho_H + \rho_L} = 0.04$), we do not use the Boussinesq approximation, which may obscure high order effects at low, but finite, A . Therefore, the density fluctuations are not neglected in the momentum equations, and the mixture density ρ and the specific volume v change in both space and time as the mass fractions evolve. We call this a variable-density (VD) flow, as opposed to the Boussinesq approximation [17, 18].

The equations describing the instability development can be derived from the compressible Navier-Stokes equations with full multicomponent diffusion by taking the limit $c \rightarrow \infty$ (c is the speed of sound) which defines the incompressible limit (see Ref. [4] for the derivation). The limiting process removes the pressure and temperature gradient effects, so that the diffusion

operator becomes Fickian in the resulting incompressible equations. Since no other assumption is imposed, the resulting equations are non-Boussinesq. One consequence is that the divergence of velocity is not zero; the energy equation as well as the species transport equations lead to a formula for the velocity divergence in terms of the derivatives of the density field.

The variable-density equations have been used in several previous studies [4,17,19–22]. In nondimensional form, they are

$$\frac{\partial}{\partial t}\rho + (\rho u_j)_{,j} = 0, \quad (2.2)$$

$$\frac{\partial}{\partial t}(\rho u_i) + (\rho u_i u_j)_{,j} = -p_{,i} + \tau_{ij,j} + \frac{1}{\text{Fr}^2}\rho g_i, \quad (2.3)$$

$$u_{j,j} = -\frac{1}{\text{Re}_0 \text{Sc}}(\ln \rho)_{,jj}. \quad (2.4)$$

The viscous stress is Newtonian with

$$\tau_{ij} = \frac{\rho}{\text{Re}_0} \left[u_{i,j} + u_{j,i} - \frac{2}{3} u_{k,k} \delta_{ij} \right], \quad (2.5)$$

and the diffusion coefficient \mathcal{D} is constant. Note that Eqs. (2.2)–(2.3) are the usual continuity and momentum transport equations for compressible flows. Equations (2.2)–(2.4) describe the mixing, at any density ratio, between incompressible materials or compressible materials in low-speed, low-acceleration flows, when the fluids participating in the mixing maintain quasiconstant microscopic densities. The designation of low-speed flow is in relation to the sound speed; since this does not appear in the VD equations, these equations can admit arbitrarily large velocities describing systems with correspondingly high sound speeds. If the densities of the two fluids are commensurate, then the mixture density is close to its average value, and Eqs. (2.2)–(2.4) lead to the Boussinesq approximation (see Ref. [17] for the derivation).

In Eqs. (2.2)–(2.4), u_i is the velocity in direction i , ρ is the mixture density, and p is the pressure. The mixture density varies between $\rho_L = 1$ and $\rho_H = (1 + A)/(1 - A)$. The nondimensional parameters in Eqs. (2.2)–(2.4) are the computational Reynolds number, $\text{Re}_0 = L_0 U_0 / \nu_0$, Schmidt number, $\text{Sc} = \nu_0 / \mathcal{D}$, and Froude number, $\text{Fr} = U_0^2 / (g L_0)$, where U_0 and L_0 are reference velocity and length scales, respectively, g_i are the components of the unit vector in the direction of gravity, $\mathbf{g} = (0, 0, -1)$, and the kinematic viscosity, $\nu_0 = \mu / \rho$, and mass diffusion coefficient \mathcal{D} are assumed constant. Note that, in general, the dynamic viscosity μ is a weaker function of density; the assumption ν_0 constant ensures a uniform Sc throughout the flow. The independent variables are the time t and space variables x_i . Equations (2.2)–(2.4) have periodic boundary conditions in the horizontal direction and slip wall conditions are applied in the direction of gravity.

B. Numerical methodology

All simulations presented here were performed with the CFDNS code [23]. The numerical approach is the same as that described in Ref. [18] and is summarized briefly below. For this problem, we used sixth-order compact finite differences [24] in the vertical (nonperiodic) direction and spectral differencing

in the horizontal (periodic) direction. To account for the difference in accuracy between the compact finite differences scheme and the Fourier differentiation, the grid spacing is 25% smaller in the vertical direction. For this grid size, in an incompressible isotropic homogeneous turbulence simulation, the error at the Kolmogorov microscale η is around 1% for the compact method, when ηk_{max} is maintained above 1.5 [25]. Nevertheless, since the Kolmogorov microscale is not well defined for the flow considered here, resolution studies were performed to verify that the solution was converged.

The time integration was performed with a third-order predictor-corrector Adams-Bashforth-Moulton method coupled with a pressure projection method, similar to Refs. [20,21]. The main difference is how the pressure equation was handled. The variable density equations lead to a variable coefficient (nonlinear) Poisson equation for pressure, as shown in Ref. [17]. This equation can be split into an explicit equation for the dilatational component of $\nabla P / \rho$, which is related to mass conservation, and an implicit equation for the solenoidal (curl) component of $\nabla P / \rho$, which is related to the baroclinic term in the vorticity equation [17,22]. Instead of interpolating the velocity from the previous step to solve the pressure equation, as done in Refs. [20,21], the pressure equation is solved without additional approximations. This avoids the introduction of errors that are the same order as the interpolation method in both mass conservation and baroclinic production of vorticity.

In this paper, only 2D simulations are considered. In all simulations, $\text{Sc} = 1$ and the Froude number is chosen such that the mesh Grashoff number [20], $\text{Gr}_\Delta \equiv 2Ag\Delta_h^3/\nu_0^2$, is below 1 (a value of 0.88 was used in simulations), to ensure that the solution is well resolved. Here, Δ_h is the mesh size in the horizontal direction and the mesh size in the vertical direction is $\Delta_v = 0.8\Delta_h$. The Atwood number in most of the simulations presented here is $A = 0.04$. One simulation was also performed at $A = 0.155$, in order to compare the results to the experiment of Waddell *et al.* [7].

The density is initialized to follow an error function profile in the vertical direction, which is consistent to the solution to the pure diffusion equation:

$$\rho = 0.5 \{1 + \text{erf}[Y_v z + \zeta(x)]\} (\rho_H - \rho_L) + \rho_L, \quad (2.6)$$

with the slope coefficient Y_v chosen such that eight grid points lie across the initial diffusion layer. For the 2D case considered here, the dependence on the second horizontal direction is removed, so that the perturbation inside the error function profile ζ is given by

$$\zeta(x) = \mathcal{A} \sin\left(\frac{2\pi x}{\lambda_0}\right), \quad (2.7)$$

where \mathcal{A} and λ_0 are the amplitude and wavelength of ζ . Note that the actual amplitude of the perturbation of the density profile is A/Y_v .

III. RESULTS

In this section, the main results of the paper are discussed. A perturbation Reynolds number Re_p is identified as strongly influencing the nature of instability development. The full

range of development stages is obtained at high enough perturbation Reynolds numbers and this is presented first. Thus, at large values of Re_p , a new stage, which we named chaotic development, is found at late times, after the reacceleration stage. The results show that the mean acceleration of the bubble front becomes constant during this stage, indicating quadratic growth. At lower values of this Reynolds number, the vortical interactions are inhibited, and the instability no longer reaches the later growth stages. This effect is discussed next. The last part of the results section addresses the role of the perturbation shape on the instability evolution. For single-mode RTI, formula (2.6) shows that the parameters characterizing the initial density field are the Atwood number, wavelength λ_0 , and Y_v and \mathcal{A} . Alternatively, Y_v and \mathcal{A} can be rewritten as the initial perturbation height, $\delta_p|_{t=0} = \mathcal{A}/Y_v$, and thickness of the initial diffusion layer based on the 1% density level, $\delta_v|_{t=0} = 1.645/Y_v$. The last two parameters have only been scarcely studied and, thus, are the main focus of our initial conditions study for single-mode RTI. All cases presented here have $A = 0.04$.

A. Growth stages in single-mode RTI

The development of single-mode RTI is usually divided into a number of stages, depending on which physical effect dominates the instability growth. At $Sc = 1$, we found that this development and the transition (or lack thereof) to the subsequent stages is strongly influenced by a perturbation Reynolds number, Re_p , defined by

$$Re_p \equiv \frac{\lambda \sqrt{\frac{A}{1+A}} g \lambda}{\nu}, \quad (3.1)$$

where the Atwood number dependence follows Refs. [26–28]. Figure 1 illustrates the evolution of the instability at five different Re_p , from left to right, $Re_p = 100$ (a), 210 (b), 400 (c), 1500 (d), 10 000 (e), 20 000 (f). For each Re_p , density contours at four time instances are shown. From top to bottom, $t\sqrt{Ag/\lambda} = 0, 2, 4, 6$. All the simulations start from the same initial perturbation as shown in Figs. 1(a1)–1(f1). At low Re_p , the growth is dominated by viscous diffusion even at very late times [e.g., see Fig. 1(a4)]. In contrast, at higher Re_p , the evolution at late times is dominated by complex vortical motions [e.g., see Fig. 1(f4)].

Figure 2 presents the evolution of the mixing layer width based on the 1% density level, $H_{0.01}$, which is defined as the maximum vertical distance between the points where the mean density equals $\rho_L + 0.01(\rho_H - \rho_L)$ and $\rho_H - 0.01(\rho_H - \rho_L)$ [19]. Also shown in Fig. 2 is the normalized bubble front speed, Fr_B , which is commonly called bubble Froude number in the literature [13] and defined as

$$Fr_B \equiv \frac{u_B}{\sqrt{\frac{A}{1+A}} g \lambda}. \quad (3.2)$$

At high enough Re_p values, the instability undergoes a number of stages, including a late time “chaotic” stage, when the bubble velocity fluctuates seemingly randomly around a mean trajectory, which was never studied before. However, as Re_p is lowered to small values, the later instability stages are subsequently no longer reached. To provide the full picture

of the development stages, the evolution of the instability at high Re_p is presented first, followed by a discussion of Re_p effects.

1. Growth stages at high Re_p

Assuming that the initial perturbation has small amplitude, the stages we identified in the present study as describing the velocity of the tip of the bubble at high Re_p are illustrated in Fig. 3:

- (1) DG: Diffusive growth (described by the solution to the heat equation)
- (2) EG: Exponential growth (described by the linear stability theory)
- (3) PFG: Potential flow growth (described by the potential flow theory)
- (4) RA: Reacceleration
- (5) CD: Chaotic development

As far as we know, the chaotic development stage was first mentioned in Ref. [29] and this is the first time the growth properties are discussed during this stage. The term “chaotic mixing” has also been used recently by Ramaprabhu *et al.* [15] to describe the late-time behavior of 3D single-mode RTI. However, as explained in the Introduction, there are fundamental differences between the two designations. Thus, the results in Ref. [15] show a return to constant bubble velocity (or continuous decrease in the bubble velocity) at late times and “chaotic mixing” refers to the complex behavior within each bubble or spike which, in their simulations, does not preserve the flow symmetries. We call “chaotic development” the late-time stage, seen only if Re_p is large enough, when the bubble acceleration itself fluctuates seemingly randomly around a mean positive value, corresponding to mean quadratic growth. We have also obtained a return to constant velocity growth (or velocities smaller than potential flow velocity) at small Re_p values; however, we do not call this “chaotic development.” As shown below, the flow itself should behave chaotically only between the symmetry lines associated to the initial conditions.

The transition between the stages is, in general, gradual. For example, between the EG and PFG stages, a “free fall” stage has been defined by Gardner *et al.* [30]. Below, we discuss each growth stage, with emphasis on the CD stage. The DG and EG stages are discussed in detail in the Appendix, in the Verification and Validation section; here we consider only some characteristic values defining the transition between these regimes.

DG to EG transition: It is known that the presence of mass diffusivity introduces a cutoff wavelength, λ_{cutoff} , below which the diffusive effects always dominate. For $\lambda < \lambda_{\text{cutoff}}$, the instability never develops and the mixing layer grows through pure diffusion [31]. However, even if the wavelength is larger than the cutoff, mass diffusion can still dominate at early times, under certain conditions. A rough estimate of the importance of purely diffusive effects at early times can be made by calculating the ratio of the velocities at the tip of the bubble in the DG and EG regimes, δ_v/δ_p . Using well-known analytical results for the pure diffusion equation in one dimension and assuming that the LST results hold in the EG stage, such that $\delta_p \approx \delta_p/n$, it yields that, in the DG

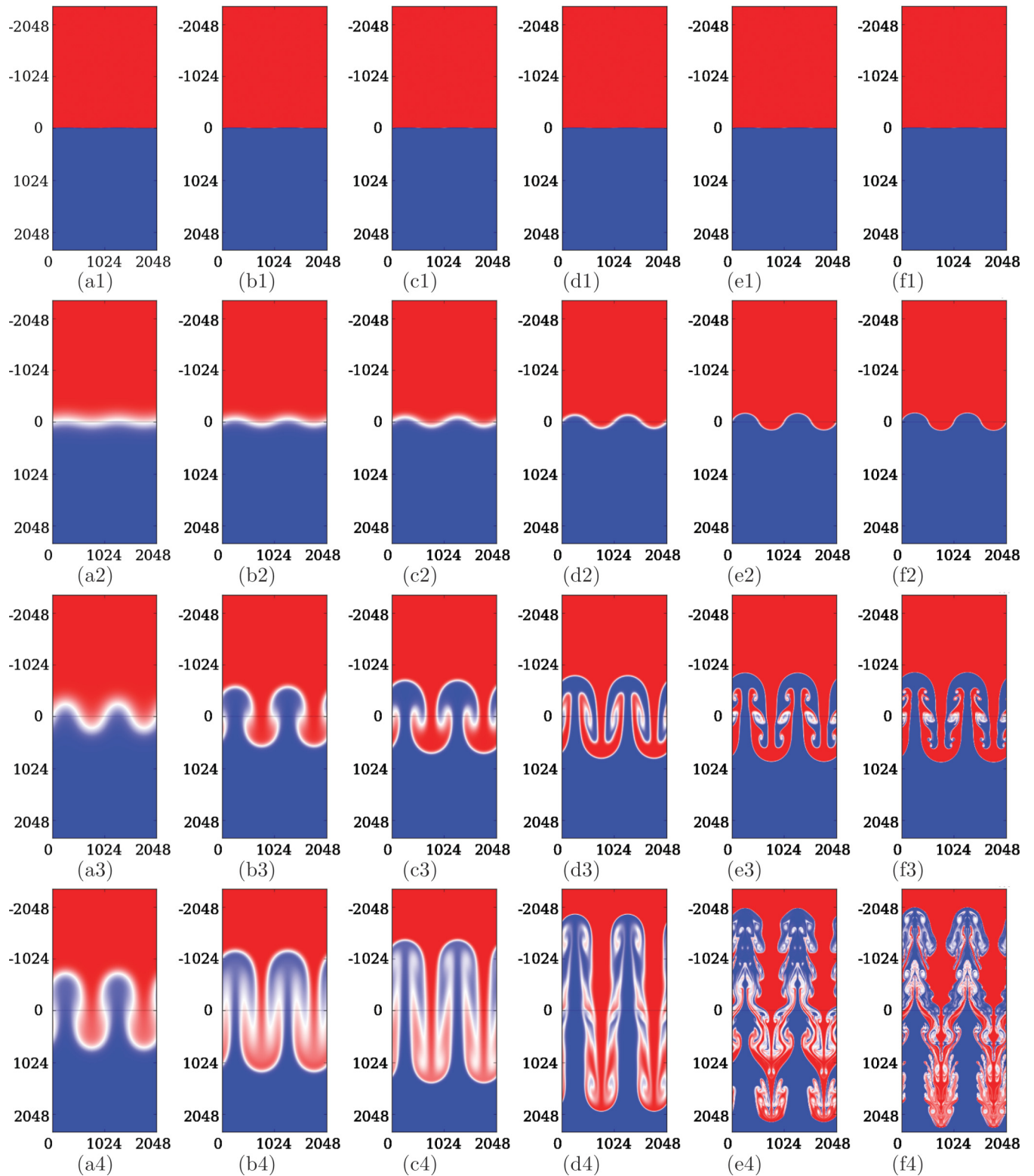


FIG. 1. (Color online) The effects of Re_p on the density contours in single-mode RTI. Red is heavy fluid, $\rho_H = 1.0833$, and blue is light fluid, $\rho_L = 1.0$. From left to right: $Re_p = 100$ (a), 210 (b), 400 (c), 1500 (d), 10 000 (e), and 20 000 (f). From top to bottom: The corresponding time instances of the density contours, given in terms of $t\sqrt{Ag/\lambda}$, are ≈ 0.0 (1), 2.0 (2), 4.0 (3), and 6.0 (4), respectively. All simulation have a horizontal size $L_h = 2048$ and grid sizes from (a) to (f): 512×3200 , 2048×7680 , 2048×7680 , 1024×6400 , 2048×7680 , and $2048 \times 12\,800$, respectively.

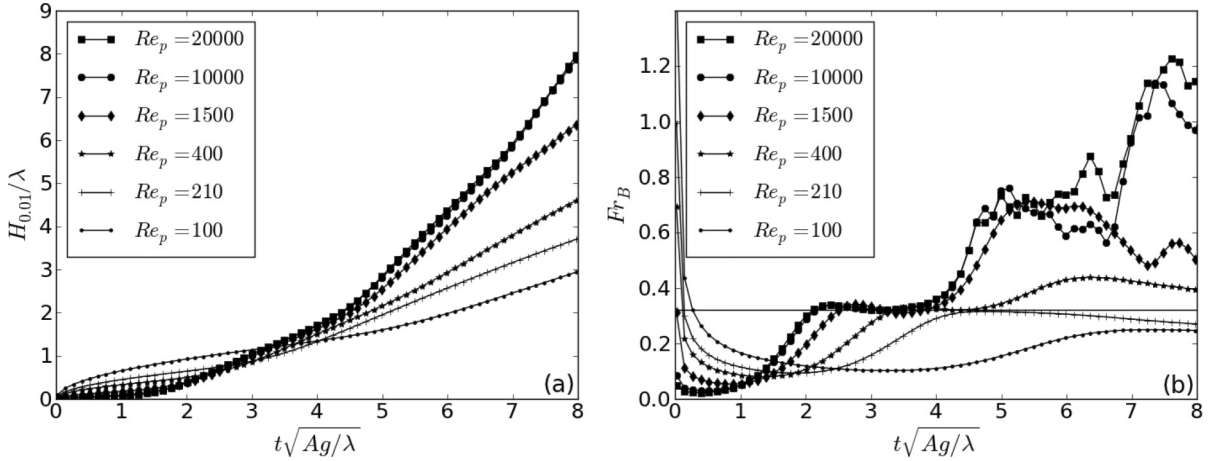


FIG. 2. The effect of perturbation Reynolds number: (a) Normalized mixing layer width and (b) normalized bubble front speed. The solid horizontal line ($Fr_B = 0.32$) represents the analytical prediction of Oron *et al.* [27] and the potential flow model of Goncharov [28].

regime:

$$\frac{\delta_v}{2(t+t_0)} \frac{1}{n\delta_p} \gg 1. \quad (3.3)$$

For the definition used, $\delta_v = H_{0.01}/2$. The DG stage condition becomes then

$$\frac{2.16}{Re_p Sc \frac{\delta_v}{\lambda} \frac{\delta_p}{\lambda} \sqrt{1 + A \frac{n}{n_I}}} \gg 1, \quad (3.4)$$

where n/n_I is the ratio between the linear growth rate in the presence of diffusive and viscous effects (A5) and the growth rate given by formula (A4). In addition, since Sc appears explicitly, one could replace the perturbation Reynolds number with a perturbation Péclet number, $Pe_p \equiv Re_p Sc$. The DG range will not occur if Pe_p and/or the layer width, due to either the perturbation amplitude or diffusion layer thickness, is large enough. Alternatively, the instability transitions to the EG stage described by the LST as the relation above is no longer satisfied due to the increase in the layer width.

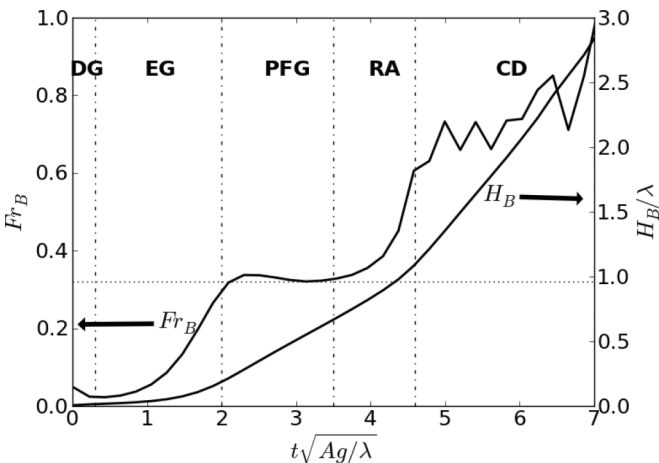


FIG. 3. Growth stages of single-mode Rayleigh-Taylor instabilities at high Re_p .

EG to PFG transition: The LST is valid as long as the nonlinear terms are negligible in the governing equations. In the present simulations, quantitative values for the bubble or spike heights (based on the 1% density values) defining the end of the EG regime are

$$H_{B/S} k \lesssim 0.67-1.33 \quad \text{or} \quad \frac{H_{B/S}}{\lambda} \lesssim 0.1-0.2. \quad (3.5)$$

With increasing the bubble and spike speed, the differential velocity on the two sides of the interfaces leads to the development of the Kelvin-Helmholtz instability on the edges of the bubbles and spikes. Initially, the wrinkle of the interface is largest near the centerline (far from the bubble and spike tip). From then on, the interface rolls up into a vortex at each intersection with the centerline and the size of each vortex grows with time. Nevertheless, not long after the nonlinear effects become important, the vortical motions generated by the Kelvin-Helmholtz instability are weak, and the flow at the tip of the bubble is still potential.

This potential flow regime is characterized by a “quasi-constant” bubble front speed. The “quasi-constant” velocity has long been observed in both experimental and numerical studies and was often called “terminal velocity” (which is misleading; see below). This was perhaps believed to be true since the vorticity itself remains zero at the tip of the bubble due to symmetry. In the previous studies, using either a drag model (e.g., Refs. [26,27]), a potential flow model (e.g., Refs. [28,32,33]), or a simple dimensional analysis, $\sqrt{g\lambda}$, has been commonly taken to characterize this “quasi-constant” bubble front speed. Irrespective of the appropriateness of the modeling assumptions, the differences among the various predictions seem to be primarily the inclusion (or not) of the dependence on density ratio and the value of the proportionality constant. Here, we compare the results with the form used in Refs. [26–28].

The drag model of Birkhoff [26] predicts a bubble velocity u_B such that $Fr_B \approx 0.35$, while the drag model of Oron *et al.* [27] and the potential flow model of Goncharov [28] both predict $Fr_B \approx 0.32$ for 2D perturbations and $Fr_B \approx 0.56$ for 3D perturbations. Our simulations exhibit Fr_B results close to these values during the PFG stage, as shown in Fig. 2. Similar

values are also reported in the recent experimental study of White *et al.* [9].

Reacceleration (RA) stage: As the fluid accelerates due to the buoyancy forces, the initial vortices grow larger and start interacting. One of the first consequences of this interaction is that the vortices split and form pairs of counter-rotating vortices (one for each bubble and spike) which start self-propelling towards the tips of the bubbles and spikes. As more vortex pairs split, the motions become more complicated; however, the first vortex pair still moves on an accelerating trajectory such that the induced velocity at the tips of the bubble or spike continues to increase. The consequence is that the velocity in these regions is no longer the solution to a potential flow problem and the tips of the bubble or spike undergo a reacceleration stage. This stage was first shown by Glimm *et al.* [12] and further discussed by Ramaprabhu *et al.* [13]. It was also confirmed experimentally in Ref. [8]. In the present simulations, quantitative values for the bubble height (based on the 1% density values) when the vortical motions start to affect the velocity of the tip of the bubble are:

$$H_B k \approx 4.7 \quad \text{or} \quad \frac{H_B}{\lambda} \approx 0.75 \quad (3.6)$$

Note that, when the vortical interactions begin to affect the velocity at the edges of the layer, the bubble and spike sides start to differentiate, even at $A = 0.04$. Since the spike side has a more complex behavior than the bubble side and is not well predicted by the potential flow theory at higher A , the estimates given here are only for the bubble side.

However, the RA stage can not last indefinitely. At most, the reacceleration lasts until the vortex pairs reach the mixing layers at the tips of the bubble or spike, so that the induced velocity can no longer increase. For the miscible case, the vortices start interacting with the mixing layer some time before their cores approach the layer edges. In addition, the continuous generation of vortical motions near the centerline, where the shearing velocity is the largest, quickly leads to complex vortical interactions, which affect the velocity induced by the first vortex pairs. Quantitative values for the end of the reacceleration stage, based on the current low A simulations, are

$$H_B k \approx 7.5 \quad \text{or} \quad \frac{H_B}{\lambda} \approx 1.2. \quad (3.7)$$

Chaotic development (CD) stage: Based on the study of vortex motions in 2D flows, Aref [34] suggested a general notion of “a threshold for chaotic behavior” in point-vortex systems. Thus, for a given flow geometry, there will be a maximum number of vortices, N_* , that can have integrable dynamics. For $N \leq N_*$, the vortex motion is at worst quasiperiodic in time. For $N > N_*$, the dynamics is chaotic with aperiodic behavior and extreme sensitivity to initial conditions. N_* is 3 for unbounded flows, but the introduction of boundaries or background potential flow in general reduces N_* .

Although the vortices in RTI are not point vortices, there are, we believe, some common features that make the Aref study relevant to the vortex motions in RTI. As shown in Fig. 1, the vortices generated above and below the original vortex core move towards the tips of the bubble or spike. These vortices subsequently break up or merge, eventually leading to complex vortical interactions. Since the induced velocity at the edges

of the layer depends on these interactions, the layer edges will undergo seemingly random acceleration and deceleration phases with varying intensity. Compounding the sensitivity of the velocities of the layer edges to the inner vortical motions is the relative weak efficiency of the instability for transforming the potential energy into vertical kinetic energy. For example, for multimode RTI, the growth is known to be quadratic, with the layer width $H \approx \alpha A g t^2$ at long times, where α is the growth coefficient and ranges from 0.02 to 0.1 in various numerical simulations and physical experiments [1,19,35]. This is much lower than the 0.5 prefactor corresponding to the free fall, so that most of the potential energy is converted into turbulent motions within the layer and is then lost through viscous dissipation. This weak efficiency is the result of friction on the sides of bubbles and spikes, with the subsequent development of the Kelvin-Helmholtz instability. A similar mechanism is present in the single-mode case and the corresponding growth rate is discussed below. A consequence of the inefficient conversion of potential into vertical kinetic energy is that the vertical development of the layer is the result of a delicate balance of terms in the mean momentum equations and the velocities of the edges of the layer are sensitive to slight changes in these terms, for example, due to the complex vortical motions. Note that our designation of “chaotic development stage” refers to the seemingly random evolution of the layer front acceleration, with its strong sensitivity to small changes in the initial perturbation shape (see below). Nevertheless, with respect to the vortical motions, even though this flow keeps the symmetries in the initial conditions, the symmetry lines act as slip walls, and the vortical motions in between these lines are also chaotic.

2. Growth stages at low Re_p

As Re_p is lowered to small values, the later instability stages: chaotic development, reacceleration, potential flow growth, and even the exponential growth described by the linear stability theory are subsequently no longer reached. Alternatively, as Re_p is increased from very small values, the instability undergoes a set of “transitions” as the layer develops and reaches the stages listed above: EG, PFG, RA, and, finally, CD. The Re_p influence on the transition to the EG stage can be inferred from formula (3.4). Below these “transitions” to subsequent stages are discussed.

“Transition” to the PFG stage: The influence of Re_p on the early development of the mixing layer can be seen from the contour plots shown in Fig. 1. The density contours in Figs. 1(a1)–1(a4) clearly indicate that, at low Re_p , the whole mixing layer is dominated by diffusive processes, including the regions near the tips of the bubble or spike. Thus, at very low Re_p , the potential flow theory can not be applied and the constant velocity stage is not observed (see Fig. 2).

With increasing the perturbation Reynolds number, the diffusive effects become less important outside the narrow interface region. Figure 2(b) shows that for $Re_p \gtrsim 200$, the instability undergoes a stage when nonlinear effects are important, yet the bubble or spike fronts are far from the influence of the initial vortex roll-up. This Re_p value is consistent with the study of Zukoski [36]. During this stage, the flow at the tips of the bubble or spike can be approximated as potential

and the velocity of the instability front approaches a plateau, with a value similar to that obtained at high Re_p (see above).

“Transition” to the RA stage: Further increasing Re_p does not change much the plateau in the velocity of the instability front (except for some minor overshoot and undershoot); however, the reduced diffusive effects allow the initial vortices to break into vortex pairs (see Fig. 1). For $Re_p \gtrsim 300$, the induced velocity generated by the vortex pairs reaccelerates the instability. If Re_p is not large enough, these vortex pairs dissipate as they approach the tips of the bubble or spike and the flow returns towards the PFG stage. It is possible that, at intermediate Re_p values, the instability will undergo multiple reaccelerations and returns to the PFG stage or simply become dominated by diffusive effects such that further vortex generation is no longer possible; however, the asymptotic time behavior was not investigated for this case.

“Transition” to the CD stage: As Re_p is increased to large values, the diffusive effects are small enough to allow complex vortical motions and interactions, with vortex break-ups and mergers. This can be clearly seen in Fig. 1: At high Re_p the mixing layer exhibits a wide range of vortical structures [e.g., see Fig. 1(f4)]. In contrast, no vortex structure exists at low Re_p . The velocity of the tips of the bubble or spike are sensitive to the induced velocities resulting from the vortical structures and, thus, are very sensitive to details of the vortical interactions. Since such complex motions have nonintegrable dynamics, the bubble or spike velocities present chaotic temporal behavior. As shown in Fig. 2, the perturbation Reynolds number for the starting of the “transition” to the CD stage is about $Re_p \approx 2000$, and the mixing layer development becomes fully chaotic for cases with $Re_p \gtrsim 10000$. The formula for the perturbation Reynolds number is similar to that which would result from the “transition” considerations made by Dimotakis [37]. Although this flow does not become turbulent, it is interesting that the Re_p values obtained for the “transition” to the CD stage are comparable to those observed in many canonical turbulent flows, as required for a fully turbulent mixing state.

B. Layer growth during the CD stage

As explained above, at high enough Re_p values, the growth rate fluctuates with time during the CD stage; however, it appears that the velocity does not fluctuate around a constant value. In order to determine the nature of the late time growth, Fig. 4(a) shows the normalized acceleration of the bubble front, $\ddot{H}_B/(2Ag)$. At late times, the acceleration becomes stationary, fluctuating around a constant value ≈ 0.035 . This indicates quadratic growth, similar to the multimode case. With this value, the mean time variation of the normalized bubble front velocity in the CD stage [Fig. 4(b)] is

$$\overline{Fr}_B \approx 0.07 t \sqrt{\frac{Ag}{\lambda}} + 0.26 \quad (3.8)$$

Note that the time when the instability reaches a mean quadratic growth depends on the initial perturbation shape (see below). The bubble front speed can also be presented as a function of the normalized bubble front height:

$$\overline{Fr}_B \approx 0.35(\sqrt{H_B/\lambda} - 1.1) + 0.5 \quad (3.9)$$

In these variables, the start of the CD stage is relatively insensitive to the initial conditions, so it was explicitly included in formula (3.9) as the 1.1 value.

These results show that there is no fundamental difference between the single-mode and multimode RTI growth, as previously believed (e.g., Refs. [32,33]). In addition, the results reconcile the apparent contradiction between the previously believed constant velocity single-mode growth and recent results showing fast quadratic growth (with α values larger than those routinely obtained in numerical simulations) for initial perturbations with a pronounced peak at $k = 1$ [3]. Therefore, single-mode RTI results could be used to understand the growth of laterally confined RTI (when the $k = 1$ mode dominates the spectrum).

For the multimode miscible case, the definition of the RTI layer width is not unique and several formulas are being used in the literature [19]. Since the value of the growth coefficient

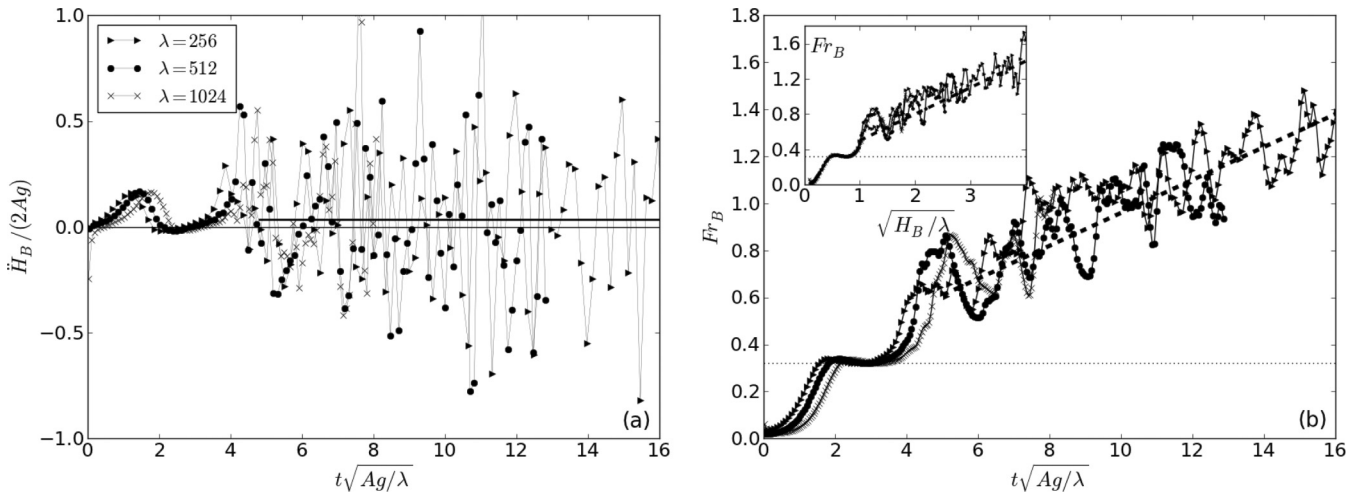


FIG. 4. Development of instability in the CD stage (at high Re_p). Results are from simulations with three wavelengths $\lambda = 256, 512, 1024$. The simulations have been run using similar computational allocations, so that the $\lambda = 256$ simulation, which uses the smallest mesh, is the longest. (a) The acceleration of the bubble front becomes stationary at late times, fluctuating around a value $\alpha_B = \overline{\ddot{H}_B}/(2Ag) \approx 0.035$ (represented by the solid horizontal line). (b) Normalized bubble front speed. The dashed straight lines are described by Eqs. (3.8) and (3.9).

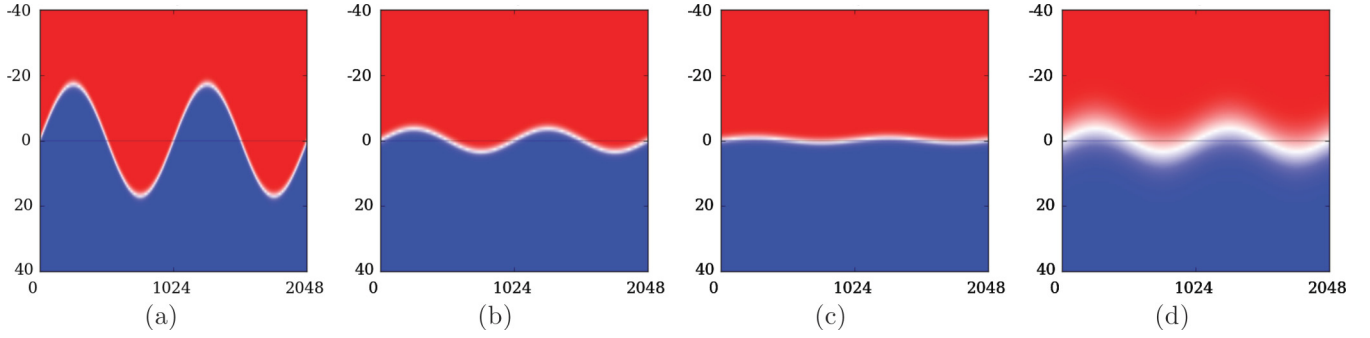


FIG. 5. (Color online) Density contours of initial perturbation shape. a–d: IC-A, IC-B, IC-C, IC-D. Red is heavy fluid, $\rho_H = 1.0833$, and blue is light fluid, $\rho_L = 1.0$. Note that the scale in the vertical direction is stretched to highlight the initial perturbation.

α depends on the definition of the layer width, in order to facilitate comparisons with the multimode case, we also give the corresponding values using the mixing layer width definitions of Cook and Dimotakis [21], $\alpha \approx 0.04$, and Youngs [38], $\alpha \approx 0.08$. The bubble height from Ref. [21] is $H_B = 1/2 \int_{-\infty}^{\infty} X_P(\bar{\rho}) dz$, where $X_P(\bar{\rho})$ is the maximum product in a fast reaction analogy (see also Ref. [39]). The bubble height from Ref. [38] is $H_B = \beta W$, where $W = \int_{-\infty}^{\infty} F_1 F_2 dz$, F_1 and F_2 are the average volume fractions of the two fluids, and the coefficient β accounts for the diffuse variation of the volume fraction near the bubble edge of the layer. Here $\beta = 3.7$ was used, which is the usual value at $A = 0.04$ in multimode simulations. While the results on the growth of 2D multimode RTI are scarce compared to the 3D literature, we note that the α values calculated above seem to be slightly larger than those reported in 2D multimode RTI simulations (e.g., Ref. [40]).

C. Effects of initial perturbation amplitude $\delta_p|_{t=0}$ and diffusion layer thickness $\delta_v|_{t=0}$

The parameters characterizing the initial density field (2.7) for single-mode RTI are the Atwood number, wavelength λ_0 , initial perturbation height, $\delta_p|_{t=0} = A/Y_v$, and the thickness of the initial diffusion layer. Based on 1% density level, this thickness is $\delta_v|_{t=0} = 1.645/Y_v$. The last two parameters have only been scarcely studied [21,41], nevertheless they can vary

widely among the experiments and numerical simulations. Thus, these parameters are the main focus of our initial conditions study for single-mode RTI.

Four different initial conditions, shown in Fig. 5, are used to study the effects of the initial perturbation shape, characterized by $\delta_p|_{t=0}$ and $\delta_v|_{t=0}$. Cases IC-A, IC-B, and IC-C have the same diffusion layer thickness ($\delta_v|_{t=0}$), but the perturbation amplitude ($\delta_p|_{t=0}$) in IC-B and IC-C is 1/5 and 1/25 that of case IC-A. Case IC-D has the same perturbation amplitude as IC-B, but five times larger diffusion layer thickness.

1. The effects of $\delta_p|_{t=0}$ and $\delta_v|_{t=0}$ at high Re_p

The effects of the initial conditions are first examined at $Re_p = 20000$, which ensures that the instability transitions into the CD stage at late time. Figure 6 shows the evolution of the mixing layer width and Fr_B for the four cases considered, and Fig. 7 shows the correspondent density contours at four time instances in the instability development, $t\sqrt{Ag/\lambda} = 0, 2, 4, 5.5$. As expected [see also formula (3.4)], both $\delta_p|_{t=0}$ and $\delta_v|_{t=0}$ affect the development at early times. Thus, the decrease in the initial layer thickness (due to both the perturbation amplitude and diffusion thickness) causes a delay in the development of mixing layer. For example, case IC-A [see Figs. 7(a1)–7(a4)] develops the fastest, followed by cases IC-B [see Figs. 7(b1)–7(b4)] and IC-D [see Figs. 7(d1)–7(d4)]

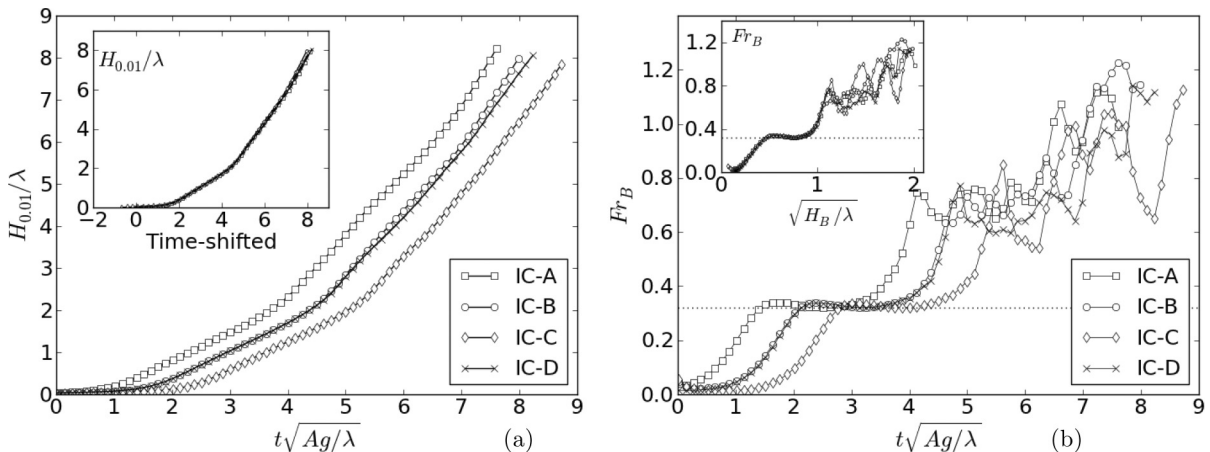


FIG. 6. The effects of the initial perturbation shape at high perturbation Reynolds number, $Re_p \approx 20000$: (a) Mixing layer width and (b) normalized bubble front speed.

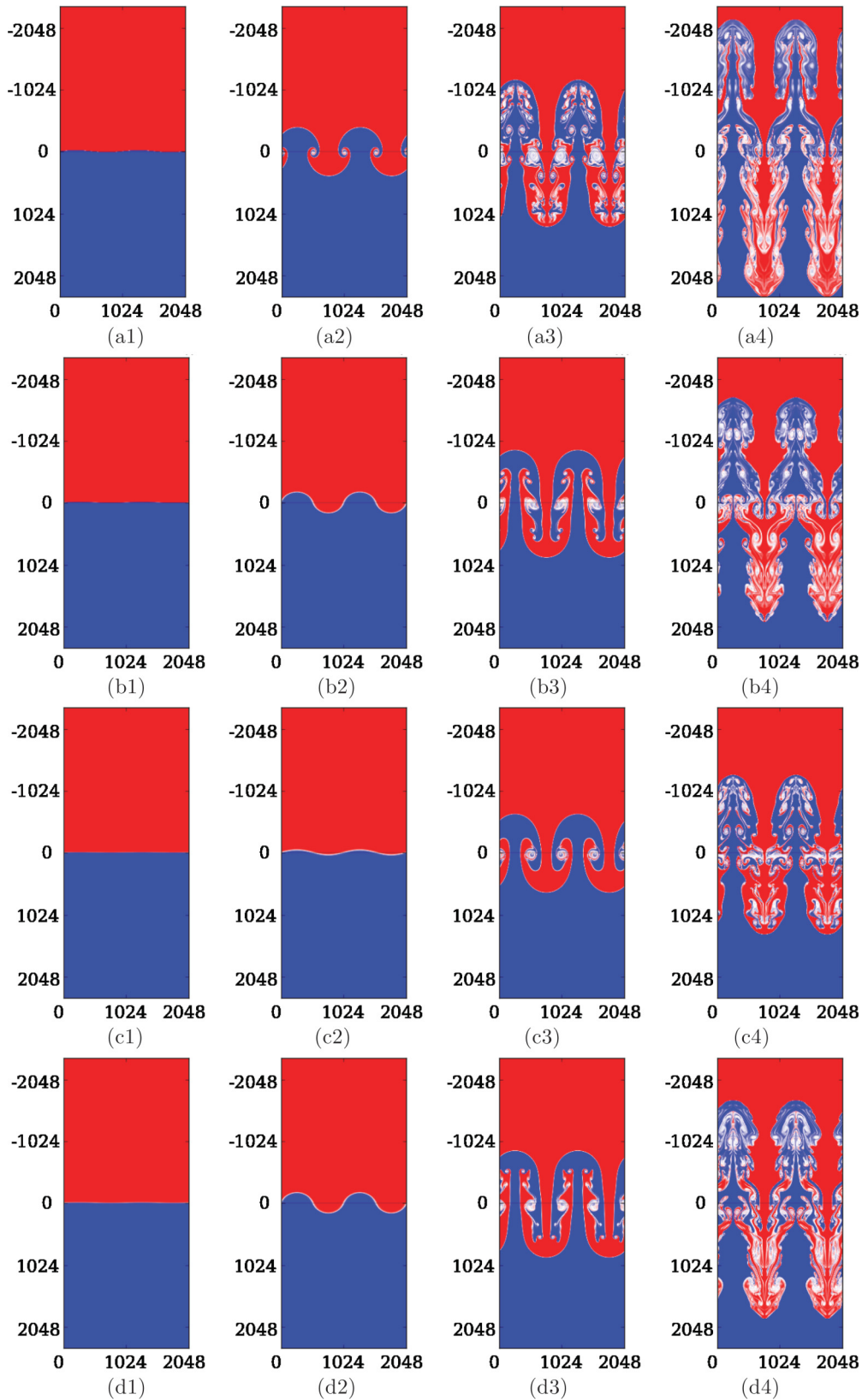


FIG. 7. (Color online) The effects of initial conditions on the density contours in single-mode RTI at high Re_p ($\approx 20\,000$). a–d: IC-A, IC-B, IC-C, IC-D. The four time instances of the density contours are 1, 2, 3, 4: $t\sqrt{Ag/\lambda} \approx 0.0, 2.0, 4.0, 5.5$. The grid size in all four simulations is 2048×12800 , corresponding to a horizontal domain size $L_h = 2048$.

which have similar evolutions, and, finally, case IC-C [see Figs. 7(c1)–7(c4)]. Nevertheless, these evolutions simply

collapse if an appropriate time shifting is used (see the inset in Fig. 6). In particular, all cases reach the same velocity during

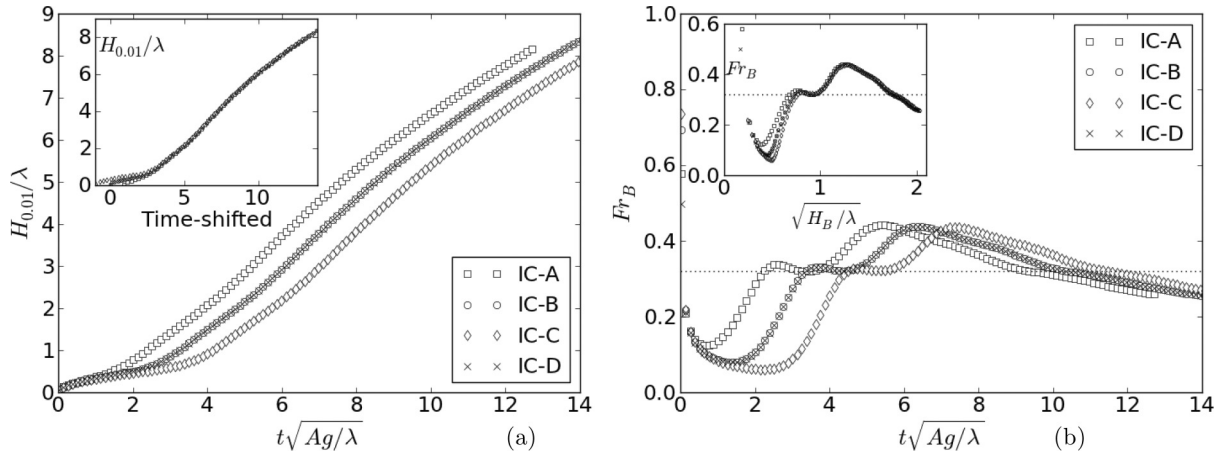


FIG. 8. The effects of initial perturbation shape at low perturbation Reynolds number, $Re_p \approx 400$: (a) Mixing layer width and (b) normalized bubble front speed.

the PFG stage so that the potential flow theory result is not affected. During the PFG stage, the flow at the tip of the bubble or spike is affected by the local interface curvature which depends on the perturbation wavelength and Atwood number, but has little influence from the initial diffusion layer thickness and perturbation amplitude.

Nevertheless, the initial vortex breakup into vortex pairs critically depends on both $\delta_p|_{t=0}$ and $\delta_v|_{t=0}$. As a result, the subsequent vortical interactions will also be very sensitive to details of the initial perturbation shape. Therefore, as the velocities of the layer edges start to be affected by the vortical motions, they become, once again, sensitive to the initial conditions, represented by $\delta_p|_{t=0}$ and $\delta_v|_{t=0}$. The strong sensitivity on the initial conditions in the CD stage can be seen in Fig. 6: The bubble front speed varies irregularly and any difference in initial conditions results in completely different instantaneous evolution of the flow.

2. The effects of $\delta_p|_{t=0}$ and $\delta_v|_{t=0}$ at low Re_p

Since at low Re_p the later stages of the instability growth are not reached (and especially the CD stage, where the initial conditions play a significant role), the effects of initial conditions are restricted to the stages where such effects can be captured through a simple time shifting (see above). Figure 8 shows that the effects of $\delta_p|_{t=0}$ and $\delta_v|_{t=0}$ on single-mode RTI at moderate Re_p , such that the CD and part of the RA stage are not reached. Indeed, the insets clearly indicate that, in this case, the mixing layer width and bubble velocity corresponding to different initial conditions collapse well with proper time shifting.

IV. SUMMARY AND CONCLUSIONS

The growth of single-mode RTI at low Atwood number ($A = 0.04$) has been investigated using DNS, with emphasis on the effects of initial conditions and Reynolds number. The findings are summarized below:

(1) Perturbation Reynolds number Re_p : A perturbation Reynolds number is identified as strongly influencing the

nature of instability development. Thus, the instability undergoes different growth stages at low and high Re_p .

(2) Growth stages: The full range of development stages is obtained at high enough Re_p . These stages are diffusional growth (DG), exponential growth (EG), potential flow growth (PFG), reacceleration (RA), and chaotic development (CD). The chaotic development stage has not been attained in the previous studies either due to too short a development time or too low a Reynolds number. The designation of “chaotic development stage” refers to the seemingly random evolution of the layer front acceleration, with its strong sensitivity to small changes in the initial perturbation shape. Thus, during this stage, the instability experiences random acceleration and deceleration phases as a result of complex vortical motions. These motions and, consequently, the bubble or spike acceleration, are very sensitive to details of the initial perturbation shape, even though the initial conditions dependence is minimal during the intermediate stages of the instability evolution. As Re_p is lowered to small values, the later instability stages are subsequently no longer reached.

(3) Transition among growth stages: As Re_p is increased from small values, the instability reaches the next development stages by undergoing a set of “transitions.”

(4) Quadratic growth in the CD stage: During the CD stage, the bubble front acceleration is stationary, such that the mean instability growth is quadratic, contrary to the general belief of late time constant velocity growth. Even though the instantaneous acceleration values are very sensitive to the initial perturbation shape, the mean value has little influence from the initial shape of the interface. The results show that the growth coefficient α_B has the approximate values 0.035, 0.04, and 0.08 for the bubble height calculated based on 1% density level, Cook and Dimotakis [21], and Youngs [38] formulas, respectively.

(5) Role of initial perturbation shape: The simulations show that the initial perturbation amplitude ($\delta_p|_{t=0}$) and diffusion thickness ($\delta_v|_{t=0}$), which characterize the initial shape of the perturbation, affect the early (DG, EG) and later stages (RA and especially CD at high Re_p). However, these parameters have a minimal role during the potential flow growth stage (PFG) and the “constant” bubble velocity prediction remains

robust for this stage. In the CD stage, the initial perturbation shape affects the instantaneous acceleration value, but this does not seem to change the mean behavior.

A. Implication for LES modeling

The perturbation Reynolds number, Re_p , has very important implications on the Large Eddy Simulations (LES) of single-mode RTI. In LES, with or without explicit subgrid scale (SGS) modeling, an “effective” perturbation Reynolds number can be defined using the SGS (or numerical) viscosity, ν_{LES} , as $\lambda\sqrt{Ag\lambda}/(1+A)/\nu_{LES}$. LES of single-mode RTI with coarse mesh may suffer from a low Re_p effect, due to an insufficient range of scales allowed by the mesh. Such an effect can be clearly seen in the ILES results of Ramaprabhu *et al.* [13] (see their Figs. 11 and 12), Glimm *et al.* [12] (their Fig. 1), Francois *et al.* [42], and Ramaprabhu *et al.* [15]. In those studies, the changing of meshes [12,13] or numerical methods [42] gave different growth rates, due to the implicit change in the effective perturbation Reynolds number. In coarse mesh (or lower effective Re_p) simulations, the later instability stages (RA and CD) were not observed. The reacceleration was observed only when the meshes used were fine enough. Even in those cases (e.g., Ref. [15]) the flow returned to bubble front velocities smaller than the potential flow result, presumably due to insufficiently high Reynolds numbers. In addition, when small-scale vortical motions were generated and seemingly influenced the growth, there is a clear interference between the physical and numerical vorticity production mechanisms, indicated by the breaking of the symmetries which should be preserved by the flow. Due to the sensitivity of the instability growth to the vortical motions, this raises significant questions on the relevance of ILES techniques to the single-mode RTI.

ACKNOWLEDGMENTS

Los Alamos National Laboratory is operated by Los Alamos National Security, LLC for the US Department of Energy NNSA under contract no. DE-AC52-06NA25396. This publication and part of the research described herein were made possible by funding from the LDRD program at Los Alamos National Laboratory through project number 20090058DR. Computational resources were provided by

LANL Institutional Computing (IC) Program and through project TUR011 on ORNL Jaguar.

APPENDIX: VERIFICATION AND VALIDATION

To verify the numerical approach, the simulation results were compared to the analytical solution to the pure diffusion equation and the linear stability theory (LST). In the nonlinear stage, the simulation results were also compared to the experimental measurements of Waddell *et al.* [7]. Finally, extensive resolution studies were performed to ensure that the solution is converged.

1. Comparison with analytical and theoretical results

Pure diffusion equation: When the mass diffusivity is large or for very small gravity or amplitude to wavelength ratio of the initial perturbation, the early flow development is dominated by diffusive effects. In this case the layer shape follows the solution to the pure diffusion equation [21]:

$$\rho = 0.5 \left\{ 1 + \operatorname{erf} \left[\frac{z}{2\sqrt{(t+t_0)/(Re_0Sc)}} \right] \right\} (\rho_H - \rho_L) + \rho_L, \quad (\text{A1})$$

with $1/[2\sqrt{t_0/(Re_0Sc)}] = Y_v$. For the layer width based on the 1% density values, the pure diffusion equation yields [21]:

$$H_{0.01}(t) \approx 6.58\sqrt{(t+t_0)/(Re_0Sc)}. \quad (\text{A2})$$

The diffusive growth stage from high diffusivity simulations is in excellent agreement with equation (A2). A separate figure is not given to show the comparison, because the diffusive growth stage is of little interest to the present study.

Linear stability theory (LST): If the initial perturbations of the interface are small, so that higher order terms can be neglected in a Taylor expansion around the unperturbed position of the interface, yet the linear buoyancy terms dominate the diffusive terms, the early flow stages can be described by the linearized form of the dynamical equations. The result is that small amplitude perturbations grow exponentially with time as

$$H(t) = h_0 \cosh(nt) + \frac{u_0}{n} \sinh(nt). \quad (\text{A3})$$

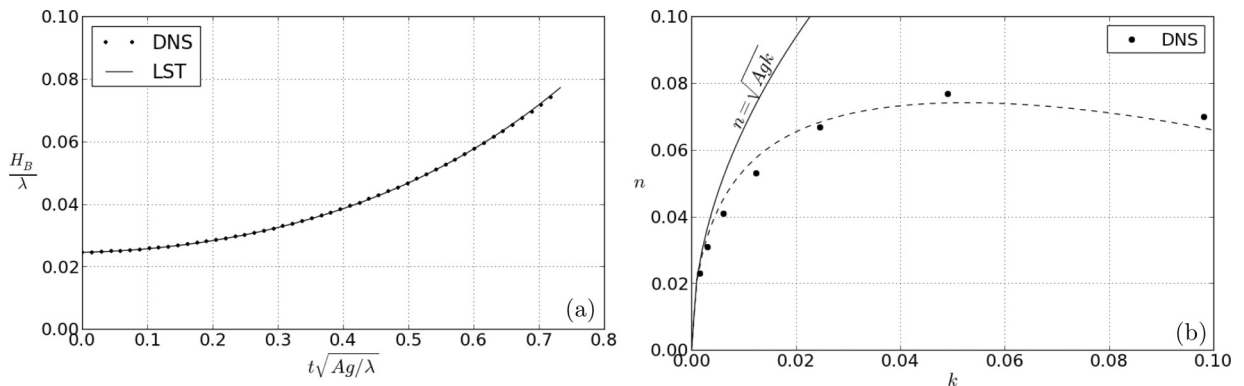


FIG. 9. Comparison between the numerical results and LST: (a) Bubble height from DNS (data points) at low wave number when the idealized LST formula (A3) (solid curve) becomes accurate. (b) Wave-number dependence of the growth rate n from simulation (data points) and the analytical approximation of Duff *et al.* [31] (dashed line). For reference, the solid curve is given by $n = \sqrt{Agk}$.

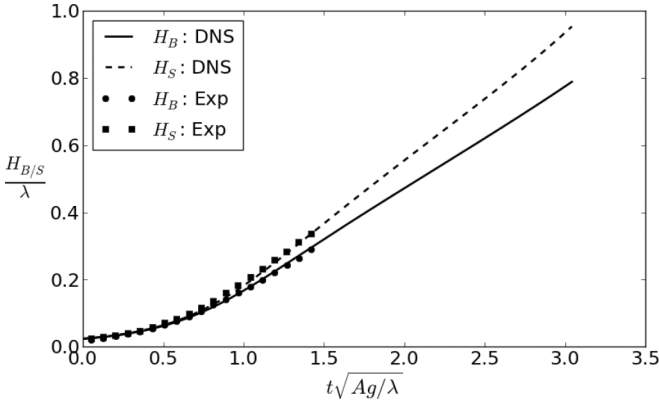


FIG. 10. Comparison between DNS results and the experiment of Waddell *et al.* [7]. The bubble, H_B , and spike, H_S , heights are calculated based on the 1% density levels and the location of the unperturbed interface, such that $H_B + H_S = H_{0,01}$.

where h_0 is the initial amplitude of the perturbation and v_0 the initial normal velocity at the interface.

In the ideal case of two incompressible immiscible inviscid fluids without surface tension, with an infinite density gradient at the interface and with an infinitesimal perturbation, the exponent in Eq. (A3) is given by the well-known formula [43]

$$n = \sqrt{Agk}, \quad (\text{A4})$$

where k is the wave number of the perturbation. For the nondimensionalization considered here, the formula reduces to $n\tau = \sqrt{L_0k}$, where $\tau = \sqrt{L_0/(Ag)}$ is the reference time scale. Additional effects, such as surface tension, viscosity, mass diffusion, gradual gradient of density, and compressibility have been studied by various authors, e.g., Refs. [31,44,45].

A comparison of the bubble amplitude growth computed from the simulation and from the analytical result (A4) is shown in Fig. 9(a), during the linear stage of the instability growth. In this case, the wave number of the perturbations is kept very small, $k = 7.67e - 4$, to minimize the diffusive effects. Figure 9(a) shows excellent agreement between the

numerical result and the analytical result. The bubble height H_B is calculated based the 1% density level.

At larger wave numbers, the diffusive effects become important and the growth rate is different than formula (A4). A good approximation for the linear stage growth rate which accounts for diffusive effects is given by Duff *et al.* [31]:

$$n = \sqrt{\frac{Agk}{\psi(A,a)} + v_0^2k^4 - (v_0 + \mathcal{D})k^2}, \quad (\text{A5})$$

where ψ is a function of A and a (here a is related to the thickness of the initial diffusive layer; see their Fig. 10). Formula (A5) gives the growth rate with about 10% accuracy. The nondimensional version of this formula is $n\tau = \sqrt{\frac{L_0k}{\psi(A,a)} + \frac{(L_0k)^2\text{Fr}^2}{A} - (1 + \frac{1}{Sc})(L_0k)^2\sqrt{\frac{\text{Fr}^2}{A}}}$. Figure 9(b) shows the wave-number variation of the numerical growth rate and the corresponding values computed with (A5). For reference, the growth rate given by formula (A4) is also shown. Figure 9(b) displays good agreement between DNS results and the analytical results of (A5).

2. Comparison with experimental results

A simulation was also carried out to match the single-mode experiment of Waddell *et al.* [7]. The materials used in the experiment are miscible and comprise of salt water and a water-alcohol solutions, resulting in $A \approx 0.155$. The simulation results agree well with the experimental measurements, as shown in Fig. 10. Note that the mixing layer width at the latest time is rather small in the experiment due to the size limitation of the experimental facility.

3. Resolution studies

To ensure that the numerical solution is fully converged, systematic mesh refinement tests have also been performed. The mixing layer width, $H_{0,01}$, and normalized bubble front speed obtained with different mesh sizes, $\Delta_h = 4.0, 2.0, 1.0$, and 0.5, are shown in Figs. 11(a) and 11(b). The results display good convergence between simulations with $\Delta_h = 2.0, 1.0$ and 0.5. The maximum relative difference in the mixing layer width

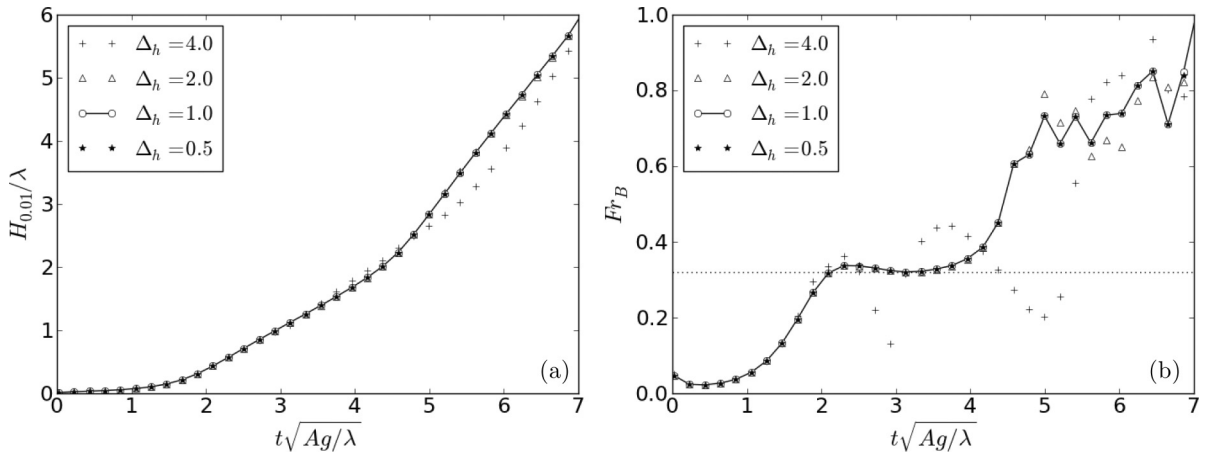


FIG. 11. Convergence of the mixing layer width and bubble front speed under grid refinement. (a) Normalized mixing layer width versus time and (b) normalized bubble front speed, Fr_B . The dashed line represents the prediction of the drag model [27] and potential flow model [28]. See Sec. III A for a discussion on these models and Fr_B definition.

values between simulations with $\Delta_h = 1.0$ and $\Delta_h = 0.5$ is smaller than 0.1% $\{|H_{\Delta_h=1.0}(t) - H_{\Delta_h=0.5}(t)|/H_{\Delta_h=0.5}(t) < 0.001\}$. In addition, the convergence rate from $\Delta_h = 2.0$ to $\Delta_h = 0.5$ is close to 6, which is the order of the method in the vertical direction. Note that the grid size in the vertical di-

rection is $\Delta_v = 0.8\Delta_h$. The simulation results reported in this paper were obtained with $\Delta_h = 1.0$. The simulations were also verified to maintain the required symmetry and yield identical results if the number of perturbation waves inside the domain and the horizontal domain size are proportionately increased.

-
- [1] G. Dimonte *et al.*, *Phys. Fluids* **16**, 1668 (2004).
- [2] N. J. Mueschke and O. Schilling, *Phys. Fluids* **21**, 014106 (2009).
- [3] D. Livescu, T. Wei, and M. R. Petersen, *J. Phys.: Conf. Ser.* **318**, 082007 (2011).
- [4] D. Livescu, *R. Soc. London Phil. Trans. A* (to be published).
- [5] P. Ramaprabhu, G. Dimonte, and M. J. Andrews, *J. Fluid Mech.* **536**, 285 (2005).
- [6] B. Rollin and M. J. Andrews, *Proceedings of the 12th International Workshops on the Physics of Compressible Turbulent Mixing, Moscow, Russia*, July (2010).
- [7] J. T. Waddell, C. E. Niederhaus, and J. W. Jacobs, *Phys. Fluids* **13**, 1263 (2001).
- [8] J. P. Wilkinson and J. W. Jacobs, *Phys. Fluids* **19**, 124102 (2007).
- [9] J. White, J. Oakley, M. Anderson, and R. Bonazza, *Phys. Rev. E* **81**, 026303 (2010).
- [10] M.-C. Renoult, R. G. Petschek, C. Rosenblatt, and P. Carles, *Exp. Fluids* **51**, 1073 (2011).
- [11] X. He, R. Zhang, S. Chen, and G. D. Doolen, *Phys. Fluids* **11**, 1143 (1999).
- [12] J. Glimm, X.-L. Li, and An-Der Lin, *Acta Mathematicae Applicatae Sinica* **18**, 1 (2002).
- [13] P. Ramaprabhu, G. Dimonte, Y. N. Young, A. C. Calder, and B. Fryxell, *Phys. Rev. E* **74**, 066308 (2006).
- [14] H. G. Lee, K. Kim, and J. Kim, *Int. J. Num. Methods Eng.* **85**, 1633 (2011).
- [15] P. Ramaprabhu, G. Dimonte, P. Woodward, C. Fryer, G. Rockefeller, K. Muthuraman, P.-H. Lin, and J. Jayaraj, *Phys. Fluids* **24**, 074107 (2012).
- [16] S. I. Abarzhi, *R. Soc. London Phil. Trans. A* **368**, 1809 (2010).
- [17] D. Livescu and J. R. Ristorcelli, *J. Fluid Mech.* **591**, 43 (2007).
- [18] D. Livescu, J. R. Ristorcelli, M. R. Petersen, and R. A. Gore, *Phys. Scr.*, **T 142**, 014015 (2010).
- [19] D. Livescu, J. R. Ristorcelli, R. A. Gore, S. H. Dean, W. H. Cabot, and A. W. Cook, *J. Turbul.* **10**, 1 (2009).
- [20] W. H. Cabot and A. W. Cook, *Nat. Phys.* **2**, 562 (2006).
- [21] A. W. Cook and P. E. Dimotakis, *J. Fluid Mech.* **443**, 69 (2001).
- [22] D. Chung and D. I. Pullin, *J. Fluid Mech.* **643**, 279 (2010).
- [23] D. Livescu, J. Mohd-Yusof, M. R. Petersen, and J. W. Grove, Technical Report LA-CC-09-100, Los Alamos National Laboratory (2009).
- [24] S. K. Lele, *J. Comput. Phys.* **103**, 16 (1992).
- [25] M. R. Petersen and D. Livescu, *Phys. Fluids* **22**, 116101 (2010).
- [26] G. Birkhoff, in *Proceedings of XIII Applied Mathematics Symposium* (American Mathematical Society, Providence, RI, 1960), p. 55.
- [27] D. Oron, L. Arazi, D. Kartoon, A. Rikanati, U. Alon, and D. Shvarts, *Phys. Plasmas* **8**, 2883 (2001).
- [28] V. N. Goncharov, *Phys. Rev. Lett.* **88**, 134502 (2002).
- [29] T. Wei, D. Livescu, and M. Andrews, *Bull. Am. Phys. Soc.* **58**, 106 (2010).
- [30] C. L. Gardner, J. Glimm, O. McBryan, R. Menikoff, D. H. Sharp, and Q. Zhang, *Phys. Fluids* **31**, 447 (1988).
- [31] R. E. Duff, F. H. Harlow, and C. W. Hirt, *Phys. Fluids* **5**, 417 (1962).
- [32] S.-I. Sohn, *Phys. Rev. E* **67**, 026301 (2003).
- [33] S. I. Abarzhi, K. Nishihara, and J. Glimm, *Phys. Lett. A* **317**, 470 (2003).
- [34] H. Aref, *Annu. Rev. Fluid Mech.* **15**, 345 (1983).
- [35] D. Livescu, M. R. Petersen, and T. Wei, in *Proceedings of the NECD2010*, Los Alamos, NM (2011).
- [36] E. E. Zukoski, *J. Fluid Mech.* **25**, 821 (1966).
- [37] P. E. Dimotakis, *J. Fluid Mech.* **409**, 69 (2000).
- [38] D. L. Youngs, *Phys. Fluids A* **3**, 1312 (1991).
- [39] D. Livescu and J. R. Ristorcelli, *J. Fluid Mech.* **605**, 145 (2008).
- [40] W. Cabot, *Phys. Fluids* **18**, 045101 (2006).
- [41] L. F. Wang, W. H. Ye, and Y. J. Li, *Phys. Plasmas* **17**, 052305 (2010).
- [42] M. M. Francois, E. D. Dendy, R. B. Lowrie, D. Livescu, and M. J. Steinkamp, in *Proceedings of the 10th International Workshop on the Physics of Compressible Turbulent Mixing (IWPCTM10)* (2007), pp. 77–80.
- [43] G. Taylor, *R. Soc. London Proc. A* **201**, 192 (1950).
- [44] S. Chandrasekhar, *Hydrodynamic and Hydromagnetic Stability* (Dover, New York, 1981).
- [45] D. Livescu, *Phys. Fluids* **16**, 118 (2004).